Thermal conductivity of half-Heusler compounds from first-principles calculations

Junichiro Shiomi,[1,2,*] Keivan Esfarjani,[2] and Gang Chen[2,†]

[1] *Department of Mechanical Engineering, The University of Tokyo, 7-3-1 Hongo, Bunkyo-ku, Tokyo, 113-8656, Japan*

[2] *Department of Mechanical Engineering, Massachusetts Institute of Technology, Cambridge, MA 02139, USA*

(Received 16 May 2011; revised manuscript received 28 July 2011; published 28 September 2011)

We demonstrate successful application of first-principles-based thermal conductivity calculation on half-Heusler compounds that are promising, environmentally friendly thermoelectric materials. Taking the case of a *p*-type half-Heusler structure, the harmonic and anharmonic interatomic force constants were obtained from a set of force-displacement data calculated by the density functional theory. Thermal conductivity was obtained by two different methods: (1) Boltzmann-Peierls formula with phonon relaxation times calculated by either Fermi's golden rule of three-phonon scattering processes or spectral analysis of molecular dynamics phase space trajectories and (2) Green-Kubo formula for heat current obtained by equilibrium molecular dynamics simulations. The calculated temperature dependence of thermal conductivity is in reasonable agreement with experiments. The method was extended to alloy crystals assuming the transferability of interatomic force constants. By having access to accurate phonon-dependent transport properties, the contribution from an arbitral subset of phonon modes can be quantified. This helps understanding the influence of nanostructures on thermal conductivity.

DOI: 10.1103/PhysRevB.84.104302 PACS number(s): 66.70.−f, 63.20.kg, 84.60.Rb, 71.15.Mb

I. INTRODUCTION

Detailed and accurate understanding of phonon transport in semiconductors and dielectrics enables a better understanding of heat transfer in microelectronics and more superior thermoelectric materials.[1,2] Use of nanostructures with characteristic lengths that are smaller than the phonon mean paths has been shown to be particularly effective in reducing thermal conductivity.[3,4] Thermoelectrics is an application that can benefit greatly from such an approach, where an ideal material would have low thermal conductivity relative to the power factor.[5] The merit of nanostructuring lies in their potential not only to reduce the lattice thermal conductivity but also to do so without sacrificing or even enhancing the power factor by taking advantage of the difference in the mean free paths of phonons and electrons and the carrier filtering and tunneling at the interface.[6–8]

Despite the strong demand motivated by the above applications, accurate calculation of intrinsic lattice heat conduction, even for bulk monoatomic crystal, has been challenging due to its anharmonic nature. Despite the partial success of the semiempirical potentials in reproducing thermal conductivity,[9,10] as most of them are not tuned for anharmonicity, there is no assurance that they would deliver the correct microscopic picture such as the mode-dependent phonon transport properties. Challenging this situation, recently, thermal conductivity calculations from first principles have been performed by extracting anharmonic interatomic force constants (IFCs) directly from the density functional perturbation theory (DFPT) calculations, which have successfully reproduced the experimentally measured thermal conductivity of bulk monoatomic crystals, namely silicon, germanium, and diamond.[11,12]

The next nontrivial challenge now is to apply the first-principles-based approach to more complicated structures such as multiatomic crystals and alloys. Since the full DFPT calculation of these systems would demand computational resource that is too large to perform in the material design routine, we need alternative methods to extract anharmonic IFCs from first-principles calculations. We overcome this by adopting the *direct method* developed by Esfarjani and Stokes.[13,14] In this method, the anharmonic IFCs are extracted by fitting their general expression to a set of Hellman-Feynman forces due to various atomic displacements calculated by density functional theory (DFT). The fitting can be performed, in theory, for an arbitral number of force-displacement data, and thus the computational load can be tuned by compromising between the load and the accuracy of the IFCs, depending on the target of analysis. The approach has been recently shown to accurately reproduce experimentally measured bulk silicon thermal conductivity.[14]

In this study, we demonstrate application of the direct method to half-Heusler (HH) compounds. Half-Heusler compounds usually have a small band gap when the total valence electron count is 18 and exhibit promising thermopower when properly doped.[15,16] With their high thermal stability and environmental friendliness, HH compounds are attractive for solid-solid heat to electricity conversion. On the other hand, among the commonly used thermoelectric materials, they have relatively high lattice thermal conductivity in bulk form, and therefore, the reduction of lattice thermal conductivity is a key issue to further enhance their figure of merit. Recently, such aspect has been explored by nanostructuring the HH compounds, which has achieved a nondimensional figure of merit (ZT) of 1.0 for *n*-type (600–700 °C)[17] and 0.8 (700 °C) for *p*-type[18] materials.

Here, we present the case of the ZrCoSb HH compound, which has been shown to be a promising base material for *p*-type thermoelectrics.[18,19] Based on the anharmonic IFCs extracted from DFT calculations, thermal conductivity was calculated via the Boltzmann-Peierls formula with phonon relaxation time calculated either by Fermi's golden rule of three-phonon (normal and umklapp) scattering processes or by spectral analysis of atomic trajectories obtained from equilibrium molecular dynamics (EMD) simulations, using potentials obtained from DFT calculations. Thermal conductivity was also directly calculated by using the

Green-Kubo formula for heat current from EMD simulations. The approaches are validated by a comparative study among the different methods and also with reported experimental data. EMD simulations further allow us to investigate the mass-difference scattering effects in alloyed HH compound, which is demonstrated here by performing thermal conductivity calculations of various ZrCoSb based alloy materials. The overall result reveals the mode-dependent phonon relaxation time and contribution to thermal conductivity, which are useful for designing thermoelectric materials in forms of alloys and nanocomposites.

II. METHODOLOGY

A. Interatomic force constants

Accurate anharmonic IFCs are crucial for thermal conductivity calculations. Particularly for thermoelectric materials, the demand for accuracy is high since thermal conductivity, by inverse proportionally influencing the figure of merit, sensitively impacts the energy conversion efficiency. To this end, we take nonempirical approach based on first-principles calculations. The first-principles calculations of cubic IFCs have become accessible even to nonspecialists through distributed codes[20] that use the DFPT method. The DFPT method finds IFCs of crystals through the $2n+1$ theorem,[21] e.g., cubic IFCs can be calculated from the linear response of the wave function. On the other hand, in the current study, for the sake of applicability to complex thermoelectric materials as discussed above, we have adopted the direct method.[13,14] The direct method finds IFCs from the variation of Hellmann-Feynman forces due to the displacements of atoms from their equilibrium positions.

The ground state energy of a crystal can be expressed in terms of IFCs by Taylor expanding about the equilibrium configuration,

$$V = V_0 + \sum_{\eta l\alpha} \Pi^{\alpha}_{\eta l} u^{\alpha}_{\eta l} + \frac{1}{2!} \sum_{\eta l\alpha,\eta' l'\beta} \Phi^{\alpha,\beta}_{\eta l,\eta' l'} u^{\alpha}_{\eta l} u^{\beta}_{\eta' l'} + \frac{1}{3!} \sum_{\eta l\alpha,\eta' l'\beta,\eta'' l''\gamma} \Psi^{\alpha,\beta,\gamma}_{\eta l,\eta' l',\eta'' l''} u^{\alpha}_{\eta l} u^{\beta}_{\eta' l'} u^{\gamma}_{\eta'' l''} + \cdots, \quad (1)$$

where the indices denote the ηth atom in lth primitive cell. The subscripts α, β, and γ label the direction of the Cartesian displacement u from the equilibrium position. Φ and Ψ are the harmonic and cubic IFCs, respectively. The residual force Π is zero as V is expanded around the minimum energy configuration. This can be rewritten in terms of forces as

$$F^{\alpha}_{\eta l} = -\Pi^{\alpha}_{\eta l} - \sum_{\eta' l'\beta} \Phi^{\alpha,\beta}_{\eta l,\eta' l'} u^{\beta}_{\eta' l'} - \frac{1}{2!} \sum_{\eta' l'\beta,\eta'' l''\gamma} \Psi^{\alpha,\beta,\gamma}_{\eta l,\eta' l',\eta'' l''} u^{\beta}_{\eta' l'} u^{\gamma}_{\eta'' l''} + \cdots \quad (2)$$

By fitting this to a set of DFT calculations of a supercell with various atomic displacements, the anharmonic IFC matrix can be systematically calculated. Although, in the current study, we have considered only up to the cubic terms, the method allows us to extend it to higher-order terms, with relatively small additional effort and computational load, which is a merit of the current direct method over the alternative DFPT method. The ranges of IFCs (number of neighboring shells of a given atom ηl) were assumed to be smaller than the supercell length and chosen separately for harmonic and cubic IFCs to minimize the fitting residual within the computationally affordable range. In the current work, we have included five and two neighboring shells for harmonic and cubic IFCs, respectively.

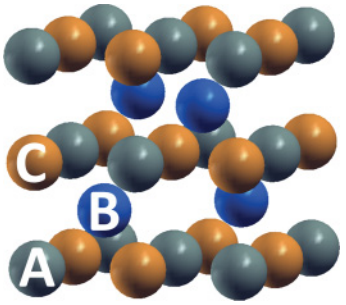

FIG. 1. (Color online) The convectional unit cell of HH compound. A primitive cell consists of three atoms A, B, and C. For ZrCoSb HH compound, A = Zr, B = Co, and C = Sb.

A set of total energy calculations with different atomic displacements was performed for a supercell of a ZrCoSb HH. A HH compound has a cubic structure consisting of three interpenetrating face-centered-cubic sublattices and one vacant sublattice.[22] As drawn in Fig. 1, the conventional unit cell of a HH compound contains four primitive cells, each of which contains three atoms. In this study, we take a cubic supercell of a $2 \times 2 \times 2$ conventional unit cell, which consists of 96 atoms in total. The DFT calculations were performed using the VASP code under the generalized gradient approximation (GGA) for the electron exchange-correlation potential, with projector-augmented-wave (PAW) pseudopotentials.[23] The GGA uses the parameterization of Perdew-Wang (GGA-PW91).[24] A $4 \times 4 \times 4$ Monkhorst-Pack[25] mesh was used to sample electronic states in the first Brillouin zone, and an energy cutoff of 400 eV was used for the plane-wave expansion, which were confirmed to give convergence of phonon properties to sufficient extent.

The force-displacement data sets were obtained by systematically displacing one or two atoms at a time about its equilibrium position along Cartesian coordinates. Note that, as described in Eq. (2), the extraction of harmonic and cubic IFCs requires at least displacements of one and two atoms, respectively. Similarly, for each irreducible degree of freedom, an atom was displaced by $\pm\Delta$r and $\pm 2\Delta$r, where Δr is 0.01 Å. While the method in theory could work with any number of force-displacement data due to its fitting nature, in the current work, displacements in all the irreducible degrees of freedom were performed taking the symmetry into account. Once we have a set of force-displacement data, together with the symmetry properties, translational and rotational invariance conditions, Eq. (2) can be fitted by using a singular value decomposition algorithm to obtain harmonic and cubic IFCs.[13]

B. Lattice dynamics

Once the harmonic IFCs are obtained, the dynamical matrix for given wave vector $\mathbf{q}$ can be computed straightforwardly by Fourier transformation.[26]

$$\tilde{D}^{\alpha\beta}_{\eta\eta'}(\mathbf{q}) = \frac{1}{\sqrt{M_\eta M_{\eta'}}} \sum_{l'} \Phi^{\alpha,\beta}_{\eta 0,\eta' l'} e^{i\mathbf{q}\cdot\mathbf{R}_{l'}}, \tag{3}$$

where M and $\mathbf{R}$ are atomic mass and position of the primitive cell, respectively.

HH crystals are polar semiconductors, and the Born effective charges are expected to influence the eigenvalues near the Γ point, which would typically result in a redshift of the longitudinal optical (LO) mode away from the transverse optical (TO) mode (LO-TO splitting). This aspect was approximated by adding the so called nonanalytical term[27] to the dynamical matrix $\tilde{D}$ obtained from the fit to first-principles forces,

$$D^{\alpha\beta}_{\eta\eta'}(\mathbf{q}) = \tilde{D}^{\alpha\beta}_{\eta\eta'}(\mathbf{q}) + \frac{4\pi}{\sqrt{M_\eta M_{\eta'}}\Omega_0} \frac{[\mathbf{q}\cdot\mathbf{Z}^*_{\eta,\alpha}][\mathbf{q}\cdot\mathbf{Z}^*_{\eta',\beta}]}{\mathbf{q}^T\boldsymbol{\varepsilon}\mathbf{q}} e^{-\frac{\mathbf{q}^2}{\rho^2}}, \tag{4}$$

where $\mathbf{Z}^*$, $\boldsymbol{\varepsilon}$, and Ω_0 are the Born effective charge, dielectric constant, and primitive cell volume, respectively. The window parameter ρ (=0.35) was set so that the nonanalytical term becomes negligible at the zone boundaries. From the dynamical matrix, we are able to calculate the harmonic properties such as eigenvalues and eigenfunction. Note that the current framework calculates ground-state properties for simplicity, although ways to calculate anharmonic phonon spectra based on first principles have been recently developed.[28]

Having access to the cubic IFCs allows us to compute the mode Grüneisen parameters, which is a useful measure of the anharmonicity of the crystal. Mode Grüneisen parameters, the change in the phonon-mode frequency with crystal volume, can be calculated as[29]

$$\gamma_G(\mathbf{q}s) = \frac{1}{6\omega^2_{\mathbf{q}s}} \sum_{\eta' l'} \sum_{\eta'' l''} \sum_{\alpha\beta\gamma} \Psi^{\alpha,\beta,\gamma}_{\eta 0,\eta' l',\eta'' l''} \frac{e^\alpha_\eta(\mathbf{q}^* s) e^\beta_{\eta'}(\mathbf{q}s)}{\sqrt{M_\eta M_{\eta'}}} \times \exp(i\,\mathbf{q}\cdot\mathbf{R}_{l'})\mathbf{r}_{l''\eta''\gamma}, \tag{5}$$

where e and $\mathbf{r}$ are the polarization vector component and equilibrium atomic position.

The cubic IFCs also allow us to calculate three-phonon scattering processes, a dominant source of intrinsic thermal resistance. This is commonly done in the (anharmonic) lattice dynamics (ALD) framework applied on cubic Hamiltonian.[30–32] By applying Fermi's golden rule to the cubic Hamiltonian in a form of phonon generation and annihilation operators, the rates of three-phonon scattering processes that satisfy the energy and momentum conservation can be expressed as

$$\Gamma_{\mathbf{q}s} = \frac{\pi\hbar}{16N} \sum_{\mathbf{q}'s'} \sum_{\mathbf{q}''s''} \frac{|\boldsymbol{A}(\mathbf{q}s,\mathbf{q}'s',\mathbf{q}''s'')|^2}{\omega_{\mathbf{q}s}\omega_{\mathbf{q}'s'}\omega_{\mathbf{q}''s''}} [(n_{\mathbf{q}'s'} + n_{\mathbf{q}''s''} + 1) \times \delta(\omega_{\mathbf{q}s} - \omega_{\mathbf{q}'s'} - \omega_{\mathbf{q}''s''}) + (n_{\mathbf{q}'s'} - n_{\mathbf{q}''s''}) \times \{\delta(\omega_{\mathbf{q}s} + \omega_{\mathbf{q}'s'} - \omega_{\mathbf{q}''s''}) - \delta(\omega_{\mathbf{q}s} - \omega_{\mathbf{q}'s'} + \omega_{\mathbf{q}''s''})\}], \tag{6}$$

where s, ω, and n are the branch index, frequency, and Bose Einstein distribution of phonons. N and $\hbar$ are the number of modes in Brillouin zone and Planck's constant. The delta function imposes the energy conservation of the three-phonon scattering processes. The three-phonon matrix element $\mathbf{A}$ is given by

$$\boldsymbol{A}(\mathbf{q}s,\mathbf{q}'s',\mathbf{q}''s'') = \sum_{\eta 0} \sum_{\eta' l'} \sum_{\eta'' l''} \sum_{\alpha\beta\gamma} \Psi^{\alpha\beta\gamma}_{\eta 0,\eta' l',\eta'' l''} \times \frac{e_{\alpha\eta}(\mathbf{q}s) e_{\beta\eta'}(\mathbf{q}'s') e_{\gamma\eta''}(\mathbf{q}''s'')}{\sqrt{M_\eta M_{\eta'} M_{\eta''}}} \times e^{i\mathbf{q}'\cdot\mathbf{R}_{l'} + i\mathbf{q}''\cdot\mathbf{R}_{l''}} \delta_{\mathbf{q}+\mathbf{q}'+\mathbf{q}'',\mathbf{G}}. \tag{7}$$

The delta function describes the momentum conservation during the normal ($\mathbf{G} = 0$) and umklapp ($\mathbf{G} \neq \mathbf{0}$) processes, where $\mathbf{G}$ is the reciprocal lattice vector. The calculation was performed for a discrete set of $\mathbf{q}$ determined by $n_k \times n_k \times n_k$ mesh covering the first Brillioun zone. Once $\Gamma_{\mathbf{q}s}$ is obtained, the phonon relaxation time can be found by $\tau_{\mathbf{q}s} = (2\Gamma_{\mathbf{q}s})^{-1}$.

C. Molecular dynamics

Once the potential function Eqs. (1) and (2) is obtained, classical EMD simulations can be performed within Newtonian dynamics. Using EMD simulations, thermal conductivity can be calculated either from the phonon relaxation time by modal analysis of the phase space trajectories or directly from the Green-Kubo formula. Thermal conductivity calculations from EMD simulations do suffer from inherent statistical uncertainty due to thermal noise and, thus, typically become more computationally demanding than the ALD method to achieve the same level of certainty. However, it has some advantages, depending on the target of analysis. One is the extendibility to complex systems, for instance, alloy crystals as will be explored later, where the ALD would need to deal with complicated eigenmodes. The other is, although not explored in the current work, the possibility of incorporating the higher-order events whose implementation is far simpler than the ALD.

Phonon relaxation times can be computed from (1) mode-dependent total energy relaxation obtained by projecting the phase space atom trajectories onto phonon eigenmodes[33] or (2) from the linewidths of the phonon spectral energy density (SED).[34–37] While the two methods deliver the same results when performed for the modes in the entire Brillouin zone of a bulk material,[38] we have chosen the latter method for its simplicity as discussed in the following.

The phonon SED is calculated by taking the power spectral density of atomic velocity[34] as

$$E(\nu,\mathbf{q}) = \left\langle \sum_{\alpha\eta} M_\eta \left| \sum_l e^{-i\mathbf{q}\cdot\mathbf{R}_l} \int \upsilon^\alpha_{\eta l}(t) e^{-2\pi i\nu t} dt \right|^2 \right\rangle. \tag{8}$$

With this, one can map the SED in frequency-wave-vector space. The scattering rate Γ can be then obtained from the half width half maximum of the Lorenzian profile fitted to each peak of the SED.[34] One can perform this analysis for the arbitral subgroup of wave vector $\mathbf{q}$, as long as the peaks are distinguishable. When the supercell is small enough, and symmetry causes enough degeneration, one could integrate

Eq. (8) over the entire wave vector domain and reduce it to the frequency-dependent SED.

$$E(\nu) = \left\langle \sum_{\alpha\eta l} M_\eta \left| \int \upsilon^{\alpha}_{\eta l}(t) e^{-2\pi i \nu} dt \right|^2 \right\rangle, \tag{9}$$

which is essentially the ensemble average of time-domain power spectral density of the atomic velocity. In this study, the overlapped multiple Lorentzian peaks were fitted all together using the Levenberg-Marquardt algorithm.[39] The SED also gives the phonon density of states by taking the area of the Lorentzian profiles. Note that the density of states here includes the frequency shifts caused by anharmonic effects at finite temperature. While this time-domain approach introduces a source of error by fitting overlapped peaks all together, it has advantages in its simplicity and in extendibility to more complex systems such as alloys, where eigenmodes take complicated forms. For the current ZrCoSb HH system, we could perform this analysis up to $n \times n \times n = 8 \times 8 \times 8$, above which the overlap of peaks were too severe for the fitting algorithm to function reasonably.

III. RESULTS AND DISCUSSION

A. Phonon dispersion relations

Figure 2(a) shows the phonon dispersion relations of ZrCoSb HH crystal along the representative symmetry lines. The three atoms in the primitive cell give rise to nine phonon branches, one longitudinal acoustic (LA), two transverse acoustic (TA), two LO, and four TO branches. The acoustic and optical branches do not overlap, but the band gaps between them are small. The Born effective charge splits the LO mode from the associated TO mode (LO-TO split) around Γ. Between the two LO branches, only the one with higher frequency at Γ point exhibits noticeable LO-TO splitting of about 50 cm^{-1}. The general features are consistent with phonon dispersion relations reported for other HH compounds such as ZrNiSn.[40] The dispersion of the highest LO mode in the off-zone center region depends on the choice of ρ. Therefore, it was confirmed that the choice of ρ does not influence the phonon relaxation time and thermal conductivity in the following calculations. In fact, we find that the inclusion of the nonanalytical term itself had only negligible effects.

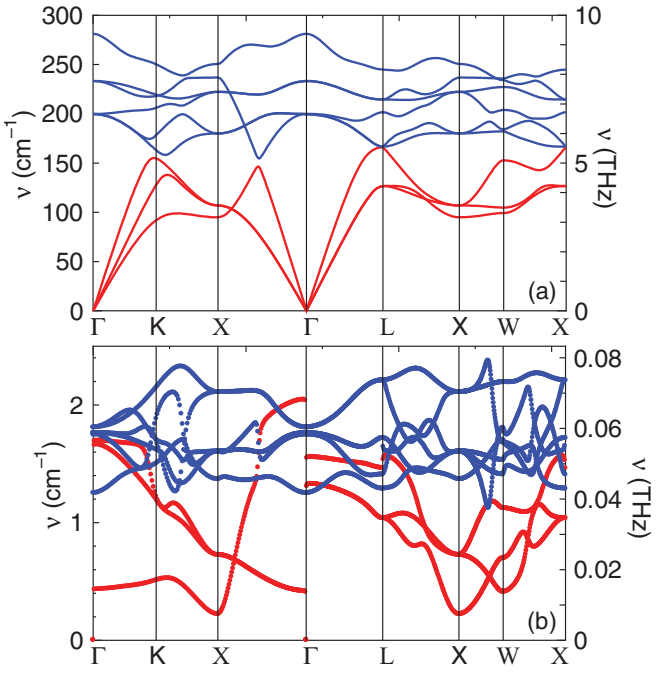

FIG. 2. (Color online) (a) The phonon dispersion relations and (b) the mode Grüneisen parameter of ZrCoSb HH compound.

The corresponding mode Grüneisen parameters γ_G in Fig. 2(b) indicate the mode-dependent strength of anharmonicity. The results show that anharmonicity, in general, is weaker for acoustic modes than for optical modes except around Γ point, where acoustic mode Grüneisen parameters exceed 1.5. The data at this long-wave limit also clarify the directional dependence of anharmonicity. Along Γ-X symmetry line, γ_G of LA mode is much larger than that of TA modes. On the contrary, along Γ-K, γ_G of TA modes overwhelms that of LA modes. Considering the eigenvectors of the acoustic modes, this indicates that in-phase displacement in [100] direction experiences much stronger anharmonicity than the displacement in [110] direction. This is understandable since atom B (Fig. 1) is displaced towards the vacant site for the [100] displacement, whereas it is bounded by another atom B for the [110] displacement. Note that atoms A and C form a rocksalt structure and are bounded isotropically. With the same logic, along Γ-L line, γ_G takes relatively large values for both LA and TA modes due to the unbounded [111] displacements of atom B. This confirms the task of vacant sites in HH compounds on enhancing the anharmonic effects compared with full Heusler compounds AB_2C with vacant sites filled with atom B. On the other hand, the overall magnitude of γ_G is still limited in a range comparable to Si[14] and smaller than PbTe,[41] which together with the relatively high group velocity, explains the relatively high thermal conductivity of HH among other thermoelectric materials.

B. Phonon relaxation time

The phonon-scattering rate calculations in Eq. (6) were done for isotropic $n_k \times n_k \times n_k$ mesh points uniformly distributed in the first Brillouin zone. Figure 3 shows the frequency-dependent phonon relaxation time calculated for $n_k = 14$ at 300 K. One can evidently see a continuous profile with respect to frequency despite that the trends are quite different among the modes, particularly between acoustic and optical modes. The phonon relaxation time of the acoustic phonons increases with decreasing frequency approximately as $\tau \propto \nu^{-2}$, a relation proposed by Klemens ($\tau = A_0 \omega^{-2} T^{-1}$),[42] which is widely accepted for relaxation of long-wave phonons caused by the phonon-phonon scattering at high enough temperature. The curve with $A_0 = 1 \times 10^{-18}$ K/s is indicated in Fig. 3. On the other hand, the optical phonons in overall have small phonon relaxation times with a peak at around 5 THz. It is interesting that such a trend with the peak in high-frequency regime is commonly observed for various structures.[14]

Figure 3 also shows the relaxation time calculated from the SED analysis of the atomistic velocity obtained from EMD simulations. Here, for the sake of comparison, we present

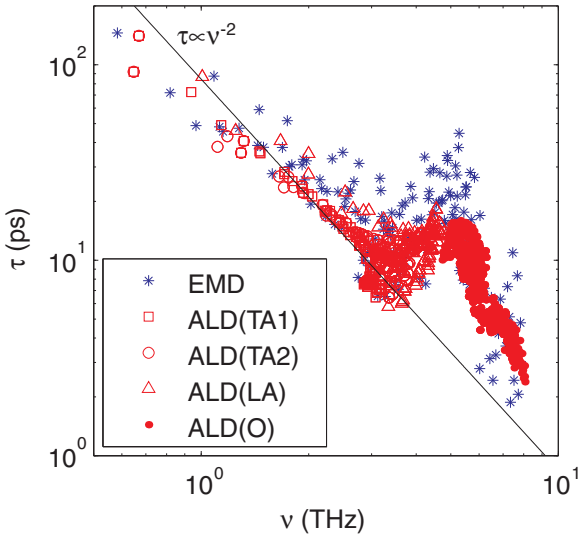

FIG. 3. (Color online) Frequency-dependent phonon relaxation time of ZrCoSb HH compound at room temperature obtained by EMD and ALD calculations. The ALD data are assigned to TA, LA, and optical (O) branches.

phonon relaxation times from $n = 8$ supercell (6144 atoms) EMD calculations, which have effectively a similar number of wave vector points as $n_k = 14$ in the ALD calculations. Although the EMD data are scattered due to the inherent thermal noise, it clearly shows quantitative agreement with the lattice dynamics results. Note that the relaxation times are not assigned to branches in this case, as we adopted the temporal SED approach. The agreement of the two methods assures the credibility of the time-domain SED analysis for phonon relaxation time extraction.

C. Lattice thermal conductivity

By using the phonon relaxation times obtained by ALD, thermal conductivity was calculated based on the relaxation time approximation.

$$\kappa = \frac{1}{3\Omega}\sum_{\mathbf{q}s} C(\omega_{\mathbf{q}s})\upsilon^2_{\mathbf{q}s}\tau_{\mathbf{q}s}, \tag{10}$$

where $C = \hbar\omega_{\mathbf{q}s}\,\partial n(\omega_{\mathbf{q}s})/\partial T$ is the mode heat capacity with Bose-Einstein distribution n, and Ω is the crystal volume. Since the finite periodic cell calculation cannot account for phonons with wavelength longer than the supercell length, whose mean paths are expected to be long, the size effect needs to be taken into account. One reasonable assumption here is that the size effect primarily comes from the missing thermal conductivity contribution from the long-wave acoustic phonons. Then if we further assume these phonons have (1) frequency $\omega \ll k_B T/\hbar$, (2) branch-dependent constant group velocity $\upsilon_{0,s}$, and (3) branch-dependent quadratic density of states $D_s = D_{0,s}\omega^2$, together with the scaling $\tau = A_0\omega^{-2}\,T^{-1}$, the size effect of thermal conductivity at certain temperature should follow,

$$\begin{aligned}\kappa(T) &= \frac{1}{3}\sum_s \int_{\omega_{\min,s}}^{\omega_{\max,s}} C(\omega,T)D_s(\omega)\upsilon_s^2(\omega)\tau_s(\omega,T)d\omega \\ &\approx \kappa_0(T) - \frac{1}{3}\sum_{s=1}^{3}\int_0^{\omega_{\min,s}} \frac{k_B D_{0,s}\upsilon_{0,s}^2 A_{0,s}}{T}d\omega \\ &= \kappa_0(T) - \frac{\pi k_B}{3an_kT}\sum_{s=1}^{3} D_{0,s}\upsilon_{0,s}^3 A_{0,s},\end{aligned} \tag{11}$$

where a is the lattice constant. Hence, in the temperature regime with dominant phonon-phonon scattering ($\kappa_0 \sim T^{-1}$),

$$\frac{\kappa(T)}{\kappa_0(T)} = 1 - \frac{c_0}{n_k}, \tag{12}$$

where c_0 is a constant. With this, the thermal conductivities calculated for $n_k = 8$, 10, 12, and 14 were extrapolated with respect to ${n_k}^{-1}$ for each temperature. As shown in the subset of Fig. 4, the size effect agrees with the linear trend in Eq. (12) with negligible fitting residuals. The obtained bulk thermal conductivity in Fig. 4 confirms $\kappa \sim T^{-1}$ in the current temperature range (100 K $< T <$ 1000 K), a typical trend in a crystal dominated by intrinsic phonon-phonon scattering.

Thermal conductivity was also calculated from EMD simulations at 300 K using the Green-Kubo formula,

$$\kappa = \frac{1}{3k_B\Omega T^2}\left\langle \int_0^\infty \boldsymbol{J}_q(0)\cdot\boldsymbol{J}_q(t')dt' \right\rangle. \tag{13}$$

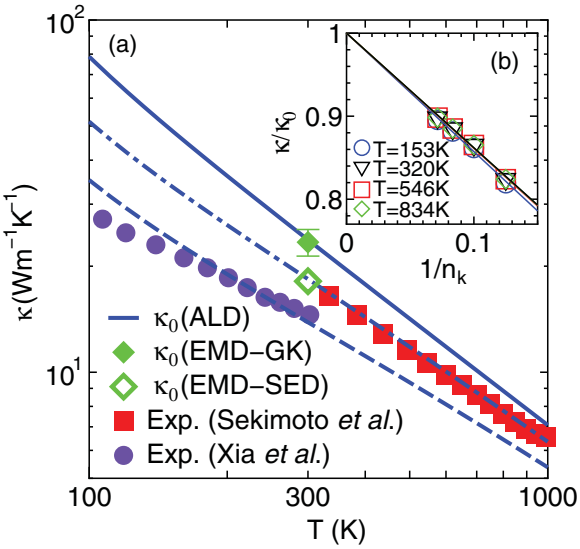

FIG. 4. (Color online) (a) Temperature dependence of bulk thermal conductivity κ_0 of ZrCoSb HH compound calculated by ALD. The results are compared with the EMD at 300 K and experiments in low-[45] and high-[46] temperature regimes. SED and GK denote data from spectral energy density and Green-Kubo approaches. The parameter B denotes the strength of defect and impurity scattering in the Rayleigh-type scattering model [Eq. (16)]. The subfigure (b) shows the extrapolation of finite-nk thermal conductivity to obtain $\kappa 0$ at different temperatures, which nearly collapses on top of each other when normalized by κ_0 [Eq. (12)].

TABLE I. Thermal conductivity of ZrCoSb HH calculated by equilibrium molecular dynamics using Green-Kubo formula.

n × n × n	Number of atoms	κ ($Wm^{-1}K^{-1}$)	Standard error ($Wm^{-1}K^{-1}$)
5 × 5 × 5	1,500	22.3	±1.66
6 × 6 × 6	2,592	22.4	±2.23
8 × 8 × 8	6,144	18.4	±1.64
10 × 10 × 10	12,000	23.4	±2.03

After equilibration for 100 ps, the ensemble-averaged integral was calculated from heat flux $\mathbf{J}_q$ for one million time steps (1 ns) of 40 simulations with different initial conditions. The calculations were performed for different system sizes up to $n = 10$ supercell (12,000 atoms). As listed in Table I, the size effect is much weaker for the EMD compared with ALD, and data converge within the range of the standard error. The converged value agrees well with the ALD data (Fig. 4).

From EMD simulations, thermal conductivity can also be calculated using the time-domain SED method. In this case, the frequency space integration needs to be approximated as

$$\kappa = \frac{1}{3}\sum_s \int_{\omega_{\min,s}}^{\omega_{\max,s}} k_B D_s(\omega) v_s^2(\omega)\tau_s(\omega)\mathrm{d}\omega \approx \frac{1}{3}\int_0^{\omega_{\max}} k_B D(\omega) v_{\mathrm{eff}}^2(\omega)\tau(\omega)\mathrm{d}\omega. \quad (14)$$

Density of states $D(\omega)$ and $\tau(\omega)$ were taken directly from the SED. An alternative way to calculate $D(\omega)$ would be to use Debye approximation and average over the symmetry lines;[10] however, it turned out to be much less accurate for the current case. To obtain the effective group velocity v_{eff}^2, the magnitude of group velocity ${v_{\mathbf{q}s}}^2$ obtained from harmonic lattice dynamics calculation was averaged over the first Brillouin zone and branches as

$$v_{\mathrm{eff}}^2(\omega) = \left[\sum_{s=1}^{9} f_s(\omega)\right]^{-1} \sum_{s=1}^{9} \left\{ \frac{f_s(\omega)\sum_{\mathbf{q}s} v_{\mathbf{q}s}^2 \delta(\omega - \omega_{\mathbf{q}s})}{\sum_{\mathbf{q}s}\delta(\omega-\omega_{\mathbf{q}s})} \right\} \quad (15)$$

$$f_s(\omega) = \begin{cases} 0 & (\omega < \omega_{\min,s}) \\ 1 & (\omega_{\min,s} \leqslant \omega \leqslant \omega_{\max,s}) \\ 0 & (\omega > \omega_{\max,s}) \end{cases}.$$

The obtained thermal conductivity is in reasonable agreement with both Green-Kubo and the ALD results (Fig. 4). This gives access to an extremely simple way of probing the microscopic property of phonon transport. With a proper approximation of the frequency-dependent group velocity, one can predict thermal conductivity by looking at the temporal history without having to deal with spatial information. This is particularly useful for a lightly alloyed system, where the change in the eigenstate makes the full-modal analysis dramatically complex, while modification in the group velocity in average is expected to be minor.

Despite the agreement between ALD and EMD calculations, the difference in the size effect implies there might be more to it. The convergence of EMD thermal conductivity at small size has been observed by other researchers. For instance, thermal conductivity calculations from EMD simulations using Stillinger-Weber potential[43] have shown that a 4 × 4 × 4 supercell (512 atoms) is enough to achieve the convergence.[44] Despite the reports, it is not clear at this point the reason why thermal conductivity should converge at such small supercell sizes despite the potential contribution from phonons with wavelengths larger than the supercell length. One speculation is that there might be a counteracting mechanism that weakens the size effect; as supercell size becomes smaller, discretization of modes is expected to reduce the phonon-scattering rates due to less possible scattering process satisfying the momentum and energy conservation. This will virtually increase the thermal conductivity, and thus the size effect will have the opposite trend from the former one. Investigation of these aspects would require a systematic study on configuration dependence of thermal conductivity, which is out of scope of the current study; however, it will be explored in the future.

The bulk thermal conductivity was compared with the reported experiments that are available for low-[45] and high-[46] temperature regimes. The two sets of experimental data exhibit mismatches in the value and slope at 300 K, presumably reflecting the difference in purity and/or crystallinity of the measured samples. Note that, although experiments measured the total thermal conductivity, the contribution of electrons is expected to be small for the undoped ZrCoSb HH material with low electrical conductivity.[46] The calculated bulk thermal conductivity falls closely above the two experimental data, with better agreement to the high-temperature measurements of Sekimoto *et al.*[46] Overestimation by the calculation is reasonable since the calculations are done for pure crystal, whereas the samples in experiments are expected to contain some impurities and defects. It is also reasonable that the agreement between the calculation and experiments becomes better as temperature increases since the dominancy of the phonon-phonon scattering becomes stronger in comparison with impurity scattering. Taking these points into account, it should be fair to state that the calculated thermal conductivity is in a reasonable agreement with the experiments.

The possible cause of the moderate discrepancies between calculation and experiments and between the low- and high-temperature experiments were investigated by assuming the influence of impurity scattering. To this end, effect of impurity scattering on the phonon relaxation time was expressed as the Rayleigh-type scattering model and added following the Matthiessen's rule as

$$\frac{1}{\tau'} = \frac{1}{\tau} + B\omega^4, \quad (16)$$

where B reflects the strength of impurity scattering.[47] The calculation can be fitted separately to the temperature dependences of low- and high-temperature experiments with $B = 3.6 \times 10^{-43}$ s^3 and 9.1×10^{-44} s^3, respectively. Although this part of the analysis is no longer *first principles*, it demonstrates

that the pure crystal data obtained from first principles can be combined with a model to probe the extent of impurity scattering in the measurements.

D. Mode dependent thermal conductivity

The strong frequency dependence of phonon relaxation time (Fig. 3) gives rise to strongly multiscale nature of phonon transport. This is even more evident in phonon mean free path $\Lambda_{\mathbf{k}s}(=|v_{\mathbf{k}s}|\tau_{\mathbf{k}s})$, which varies by several orders of magnitude with respect to the phonon frequency in the current frequency range. Let us now discuss the implication this has to nanostructured materials.[6,17,18] If we consider nanostructures with characteristic length scale L, the phonons with mean free path $\Lambda \ll L$ are transported *diffusively* between the interfaces behaving similarly to those in bulk material. On the other hand, phonons with $\Lambda > L$ are transported *ballistically* between the interfaces and thus can be strongly influenced by the interface scattering. In other words, mean free paths, in a rough sense, gives a sense of the potential for the phonon transport to be affected by the nanostructures.

In this course, an important measure is the amount of contribution from phonons with various mean free paths. This can be explored by calculating the cumulative thermal conductivity with respect to the phonon mean free path[48] described as

$$\kappa_c(\Lambda_0) = \frac{1}{3\Omega} \sum_{\mathbf{q}s}^{\Lambda_{\mathbf{q}s}<\Lambda_0} C(\omega_{\mathbf{q}s}) v_{\mathbf{q}s} \Lambda_{\mathbf{q}s}. \quad (17)$$

The cumulative thermal conductivity at 300 K was calculated from ALD with $n_k = 14$ mesh. Now, extrapolation to the bulk value needs to be carried out in a similar manner as Eq. (11). By expressing Eq. (11) in terms of Λ, we obtain

$$\kappa_c(\Lambda_0) \approx \kappa_0 - \frac{k_B}{6T^{3/2}} \sum_{s=1}^{3} D_{0,s} v_{0,s}^{5/2} A_{0,s}^{3/2} \int_{\Lambda_0}^{\infty} \Lambda^{-3/2} d\Lambda$$

$$= \kappa_0 - \frac{k_B \Lambda_0^{-1/2}}{3T^{3/2}} \sum_{s=1}^{3} D_{0,s} v_{0,s}^{5/2} A_{0,s}^{3/2}. \quad (18)$$

Hence, the values calculated with finite mesh sizes can be extrapolated with the function $\kappa_c = \kappa_0 - c_1 \Lambda_0^{-1/2}$, where c_1 is a constant. As shown in Fig. 5, the cumulative thermal conductivity profile reveals that the phonons with extremely wide range (from 10 nm to 10 μm) of mean free paths have noticeable contribution to thermal conductivity.

From the cumulative thermal conductivity, one can gain insight into heat conduction in nanostructured materials. Recent experiments have shown that it is possible to nanostructure HH compounds with average grain sizes of the order of 100 nm, which has significantly enhanced the figure of merit.[18] Our calculations show that phonons with $\Lambda > 100$ nm have potential to carry 25% of the heat in a bulk material. In other words, if the interface backscattered all the ballistic phonons, the nanostructuring with length scale 100 nm would have potential to reduce thermal conductivity by quarter, which supports the large effect seen in the experiments. Of course, in reality, the effect of nanostructure would depend on the interface properties such as phonon transmission function, and thus, this analysis only gives us the upper limit of such effects. In this sense, more valuable indication from this analysis might be that there is plenty of room for further reduction of thermal conductivity by nanostructuring HH compounds.

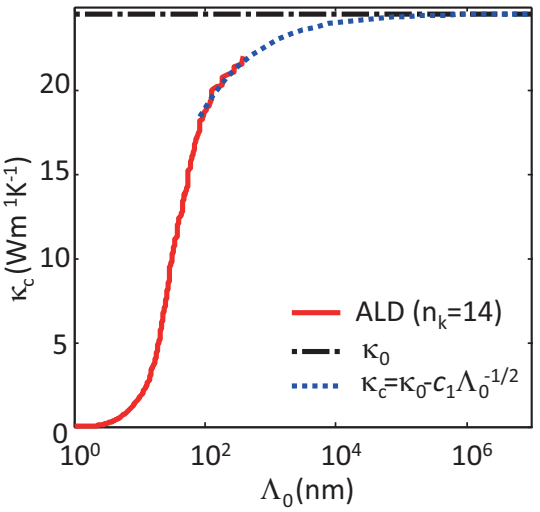

FIG. 5. (Color online) The cumulative thermal conductivity κ_c of ZrCoSb HH compound calculated by ALD and EMD calculations at room temperature. The cumulative thermal conductivity is obtained by accumulating contribution from phonons with mean free path of Λ_0 or less [Eq. (17)]. The finite size results with $n_k = 14$ are extrapolated using Eq. (18). The dash-dotted line indicates the calculated bulk thermal conductivity κ_0.

E. Extension to alloy systems

In practical situations, thermoelectric materials are often alloyed to reduce thermal conductivity and to control carrier concentration. For HH materials, thermal conductivity reduction is often realized by forming $Hf_yZr_zTi_{1-y-z}BC$.[18,19,49] Here, using EMD simulations, the alloy effects of $Hf_xZr_{1-x}CoSb$, $Zr_xTi_{1-x}CoSb$, and $Hf_{1-x}Ti_xCoSb$ are investigated by randomly alloying Hf, Zr, and Ti with fraction x based on the mass approximation concept,[50] where only the atomic masses are varied by keeping the IFCs the same. Such transferability of IFCs has been empirically shown to work between GaAs and AlAs, which have practically the same lattice parameter.[50] The lattice constant for HfCoSb, ZrCoSb, and TiCoSb are 6.06, 6.10, and 5.94 Å; therefore, we expect calculations of $Hf_xZr_{1-x}CoSb$ to be more accurate than the others. While lattice dynamics would be able to model the alloy effect based on the perturbation theory,[51–54] the EMD simulation allows us to directly calculate the thermal conductivity.

Thermal conductivity of HH alloys was calculated by Green-Kubo method for various x. The calculations were performed for two different supercell size $n = 5$ and 8, where the size effect was as small as that in the pure crystal case. For each configuration, the thermal conductivity was averaged over three different random configurations (eight simulations with different initial conductions per configuration). As shown in Fig. 6, thermal conductivity of $Zr_{0.5}Ti_{0.5}CoSb$, $Hf_{0.5}Zr_{0.5}CoSb$, and $Hf_{0.5}Ti_{0.5}CoSb$ were calculated to be 6.4, 3.3, and 1.8 W/mK, respectively. The value of $Hf_{0.5}Zr_{0.5}CoSb$ is in reasonable agreement with the lattice thermal conductivity of $Hf_{0.5}Zr_{0.5}CoSb_{0.8}Sn_{0.2}$ measured by Yan *et al.*[18] Note

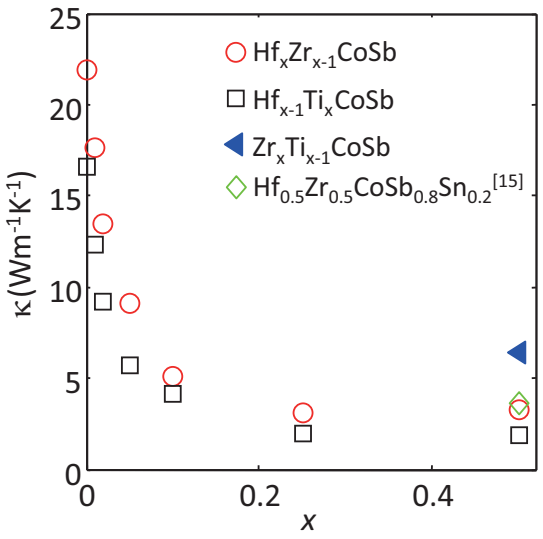

FIG. 6. (Color online) Thermal conductivity of alloyed HH compounds with various alloy fraction x. (Hf, Zr, Ti)CoSb HH alloys were modeled by assuming transferability of IFCs. The calculated values are compared an experimentally value for $Hf_{0.5}Zr_{0.5}CoSb_{0.8}Sn_{0.2}$.[18]

that mass difference scattering due to Sb-Sn substitution is expected to be minute due to their small mass difference. Figure 6 also shows thermal conductivity of $Hf_xZr_{1-x}CoSb$ and $Hf_{1-x}Ti_xCoSb$ alloys with respect to the alloy fraction x. The result shows that thermal conductivity rapidly decreases for small x and becomes modest as x increases. Such data quantitatively clarifies the sensitivity of the thermal conductivity to the alloy fraction and are useful for optimization of the alloy components.

IV. CONCLUSIONS

We have demonstrated application of first-principles-based thermal conductivity calculation on p-type half-Heusler compounds, promising next-generation thermoelectric materials. Harmonic and cubic force constants were obtained based on a set of force-displacement calculations by DFT. With the nonempirical force constants, harmonic and anharmonic phonon properties were characterized through phonon dispersion relations and mode Gruneissen parameters. Mode relaxation times were calculated by ALD and spectral density analysis of molecular dynamics phase space trajectories. They quantitatively agree with each other exhibiting key phonon transport characteristics such as inverse quadratic frequency dependence. Thermal conductivity was then calculated under the relaxation time approximation, which agrees with direct calculation using molecular dynamics and the Green-Kubo formula. By having access to accurate phonon-dependent transport properties, the contribution to heat conduction from an arbitral subset of phonon modes can be quantified, which helps understanding the influence of nanostructures on thermal conductivity. Finally, the possibility to extend the method to alloy systems has been demonstrated, showing that the current framework can be useful to characterize complicated crystal structures that often appear in thermoelectric applications and to optimize the material composition or to design new phonon-engineered crystals.

ACKNOWLEDGMENTS

The authors acknowledge discussion with Zhifeng Ren, Xiao Yan, Takuma Shiga, and Takuma Hori. This material is partially based upon work supported as part of the "Solid State Solar-Thermal Energy Conversion Center (S3TEC), an Energy Frontier Research Center funded by the US Department of Energy, Office of Science, Office of Basic Energy Sciences under Award Number: DE-SC0001299 (K.E. and G.C.), and by Japan Society for the Promotion of Science, Excellent Young Researchers Overseas Visit Program and KAKENHI 23760178 (J.S.).

*shiomi@photon.t.u-tokyo.ac.jp
†gchen2@mit.edu

[1] D. G. Cahill, W. K. Ford, K. E. Goodson, G. D. Mahan, A. Majumdar, H. J. Maris, R. Merlin, and S. R. Phillpot, J. Appl. Phys. **93**, 793 (2003).
[2] M. S. Dresselhaus, G. Chen, Ming Y. Tang, R. Yang, H. Lee, D. Wang, Z. Ren, J.-P. Fleurial, and P. Gogna, Adv. Mater. **19**, 1043 (2007).
[3] S.-M. Lee, D. G. Cahill, and R. Venkatasubramanian, Appl. Phys. Lett. **70**, 2957 (1997).
[4] D. Li, Y. Wu, P. Kim, L. Shi, P. Yang, and A. Majumdar, Appl. Phys. Lett. **83**, 2934 (2003).
[5] G. A. Slack, in *Handbook of Thermoelectrics*, edited by D. M. Rowe (CRC Press, UK, 1995), p. 407.
[6] B. Poudel, Q. Hao, Y. Ma, Y. Lan, A. Minnich, B. Yu, X. Yan, D. Wang, A. Muto, D. Vashaee, X. Chen, J. Liu, M. S. Dresselhaus, G. Chen, and Z. F. Ren, Science **8**, 4670 (2008).
[7] A. J. Minnich, M. S. Dresselhaus, Z. F. Ren, and G. Chen, Energy Environ. Sci. **2**, 466 (2009).
[8] M. G. Kanatzidis, Chem. Mater. **22**, 648 (2010).
[9] S. G. Volz and G. Chen, Phys. Rev. B **61**, 2651 (2000).
[10] A. S. Henry and G. Chen, J. Comput. Theor. Nanosci. **5**, 1 (2008).
[11] D. A. Broido, M. Malorny, G. Birner, N. Mingo, and D. A. Stewart, Appl. Phys. Lett. **91**, 231922 (2007).
[12] A. Ward, D. A. Broido, D. A. Stewart, and G. Deinzer, Phys. Rev. B **80**, 125203 (2009).
[13] K. Esfarjani and H. T. Stokes, Phys. Rev. B **77**, 144112 (2008).
[14] K. Esfarjani, G. Chen, and H. T. Stokes, Phys. Rev. B **84**, 085204 (2011).
[15] C. Uher, J. Yang, S. Hu, D. T. Morelli, and Meisner, Phys. Rev. B **59**, 8615 (1999).
[16] S. J. Poon, *Recent Trends in Thermoelectric Materials Research II, Semiconductors and Semimetals*, edited by T. M. Tritt (Academic, New York, 2001), p. 37.

[17]G. Joshi, X. Yan, H. Wang, W. Liu, G. Chen, and Z. F. Ren, Adv. Energy Mater. **1**, 643 (2011).
[18]X. Yan, G. Joshi, W. Liu, Y. Lan, H. Wang, S. Lee, J. W. Simonson, S. J. Poon, T. M. Tritt, G. Chen, and Z. F. Ren, Nano Lett. **11**, 556 (2011).
[19]S. R. Culp, J. W. Simonson, S. J. Poon, V. Ponnambalam, J. Edwards, and T. M. Tritt, Appl. Phys. Lett. **93**, 022105 (2008).
[20]P. Giannozzi, S. Baroni, N. Bonini, M. Calandra, R. Car, C. Cavazzoni, D. Ceresoli, G. L. Chiarotti, M. Cococcioni, I. Dabo, A. D. Corso, S. de Gironcoli, S. Fabris, G. Fratesi, R. Gebauer, U. Gerstmann, C. Gougoussis, A. Kokalj, M. Lazzeri, L. Martin-Samos, N. Marzari, F. Mauri, R. Mazzarello, S. Paolini, A. Pasquarello, L. Paulatto, C. Sbraccia, S. Scandolo, G. Sclauzero, A. P. Seitsonen, A. Smogunov, P. Umari, and R. M Wentzcovitch, J. Phys.: Condens. Matter **21**, 395502 (2009).
[21]X. Gonze and J.-P. Vigneron, Phys. Rev. B **39**, 13120 (1989).
[22]W. Jeischko, Metall. Trans. **1**, 3159 (1970).
[23]G. Kresse and J. Furthmüller, Comput. Mater. Sci. **6**, 15 (1994).
[24]J. Perdew and Y. Wang, Phys. Rev. B **45**, 13244 (1992).
[25]H. J. Monkhorst and J. D. Pack, Phys. Rev. B **13**, 5188 (1976).
[26]N. W. Ashcroft and N. D. Mermin, *Solid State Physics* (Saunders College Publishing, Fort Worth, 1976).
[27]K. Parlinski, Z. Q. Li, and Y. Kawazoe, Phys. Rev. Lett. **78**, 4063 (1997).
[28]P. Souvatzis, O. Eriksson, M. I. Katsnelson, and S. P. Rudin, Phys. Rev. Lett. **100**, 095901 (2008).
[29]T. H. K. Barron and M. L. Klein, in *Dynamical Properties of Solids,* Edited by G. K. Horton and A. A. Maradudin (North Holland, Amsterdam, 1974), p. 391.
[30]R. Peierls, *Quantum Theory of Solids* (Clarendon, Oxford, 1955).
[31]M. Ziman, *Electrons and Phonons* (Oxford University Press, London, 1960).
[32]G. P. Srivastava, *The Physics of Phonons* (Taylor & Francis, New York, 1990).
[33]A. J. H. McGaughey and M. Kaviany, Phys. Rev. B **69**, 094303 (2004).
[34]J. A. Thomas, J. E. Turney, R. M. Iutzi, C. H. Amon, and A. J. H. McGaughey, Phys. Rev. B **81**, 081411 (2010).
[35]C. Z. Wang, C. T. Chan, and K. M. Ho, Phys. Rev. B **42**, 11276 (1990).
[36]J. Shiomi and S. Maruyama, Phys. Rev. B **73**, 205420 (2006).
[37]N. de Koker, Phys. Rev. Lett. **103**, 125902 (2009).
[38]T. Hori, T. Shiga, S. Maruyama, and J. Shiomi, in *48th National Heat Transfer Symposium of Japan* (Okayama, Japan, 2011).
[39]M. Wojdyr, J. Appl. Crystallogr. **43**, 1126 (2010).
[40]H. Özişik, K. Çolakoğlu, and Havva Boğaz Özişik, Fizika **16**, 154 (2010).
[41]Y. Zhang, X. Ke, C. Chen, J. Yang, and P. R. C. Kent, Phys. Rev. B **80**, 024304 (2009).
[42]P. Klemens, Proc. R. Soc. **A208**, 108 (1951).
[43]F. H. Stillinger and T. A. Weber, Phys. Rev. B **31**, 5262 (1985).
[44]D. P. Sellan, E. S. Landry, J. E. Turney, A. J. H. McGaughey, and C. H. Amon, Phys. Rev. B **81**, 214305 (2010).
[45]Y. Xia, S. Bhattacharya, V. Ponnambalam, A. L. Pope, S. J. Poon, and T. M. Tritt, J. Appl. Phys. **88**, 1952 (2000).
[46]T. Sekimoto, K. Kurosaki, H. Muta, and S. Yamanaka, Jpn. J. Appl. Phys. **46**, L673 (2007).
[47]P. G. Klemens, Proc. Phys. Soc. London, Sect. A **68**, 1113 (1955).
[48]C. Dames and G. Chen, in *Thermoelectrics Handbook: Macro to Nano* (CRC Press, Boca Raton, 2005).
[49]S. Katsuyama and T. Kobayashi, Mater. Sci. Eng., B **166**, 99 (2010).
[50]P. Giannozzi, S. de Gironcoli, P. Pavone, and S. Baroni, Phys. Rev. B **43**, 7231 (1991).
[51]S. Tamura, Phys. Rev. B **27**, 858 (1983).
[52]S. Baroni, S. de Gironcoli, and P. Giannozzi, Phys. Rev. Lett. **65**, 84 (1990).
[53]N. Marzari, S. de Gironcoli, and S. Baroni, Phys. Rev. Lett. **72**, 4001 (1994).
[54]J. Garg, N. Bonini, B. Kozinsky, and N. Marzari, Phys. Rev. Lett. **106**, 045901 (2011).